

PAPER



Cite this: *J. Mater. Chem. C*, 2018, **6**, 7285

Received 9th April 2018, Accepted 13th June 2018

DOI: 10.1039/c8tc01651h

rsc.li/materials-c

Fast luminescence from rare-earth-codoped BaSiF₆ nanowires with high aspect ratios†

Gibin George, (1) a Shanell L. Jackson, a Zariana R. Mobley, Bhoj R. Gautam, Dong Fang, * Jinfang Peng, * Duan Luo, Jianguo Wen, Jason E. Davis, Daryush Ilaa and Zhiping Luo (1) *

Inorganic materials with short radiative decay time are highly desirable for fast optical sensors. This paper reports fast photoluminescence (PL) from a series of barium hexafluorosilicate (BaSiF₆) superlong nanowires with high aspect ratios, codoped with $Ce^{3+}/Tb^{3+}/Eu^{3+}$ ions, with a subnanosecond decay time. Solvothermally synthesized BaSiF₆ nanowires exhibit a uniform morphology, with an average diameter less than 40 nm and aspect ratios of over several hundreds, grown in the c-axis direction with {110} surfaces. The PL emission from the codoped BaSiF₆ nanowires, when excited by a 254 nm source, is dependent on Tb^{3+} concentration, and the energy transfer from Ce^{3+} to Tb^{3+} and to Eu^{3+} ions allows efficient emissions in the visible spectra when excited by a near UV source. Annealing BaSiF₆ nanowires at 600 °C in a vacuum produced barium fluoride (BaF₂) nanowires composed of nanocrystals. Both BaSiF₆ and BaF₂ nanowires exhibit fast emissions in the visible spectra, with enhanced intensities compared with their codoped microparticle counterparts. The decay time of codoped BaSiF₆ nanowires is found to be shorter than that of codoped BaF₂ nanowires. The energy transfer is also observed in their cathodoluminescence spectra with high-energy irradiation.

Introduction

Historically, rare-earth (RE) ions have been successfully used to dope scintillators/phosphors to ameliorate their luminescence properties. Trivalent Tb³⁺ and Eu³⁺ ions are extensively used as activators due to their characteristic green and red emission bands, respectively. Eu³⁺ ions are attractive for their intense red emission; while Eu³⁺ ions exhibit a weak and narrow absorption in the UV regions due to the narrow linewidth of Eu³⁺ 4f-4f absorption transitions and low oscillator strength. Generally, emissions from Eu³⁺ ions are enhanced by various sensitizers

such as Ce^{3+} and Eu^{2+} with 4f–5d allowed transitions, coupled with Tb^{3+} or Gd^{3+} ions as bridges to transfer the energy between Ce^{3+} and Eu^{3+} by minimizing the metal–metal charge transfer quenching, which otherwise equally quenches the emission from the sensitizer and activator ions.

Alkaline earth fluorides are reckoned as ideal hosts for a large number of inorganic scintillators/phosphors, owing to their unique chemical stability and favourable photoluminescence (PL) characteristics, such as electron-acceptor behaviour, large optical-transmission domains, high resistivity and anionic conductivity.² Among them, barium hexafluorometallates have been established as a fluorescent host matrix in the recent years, for example, BaSiF₆ (BSF),³ BaGeF₆,⁴ BaTiF₆,⁵ and BaSnF₆,⁶ doped with Mn⁴⁺ for commercial LEDs with a luminescence decay time in the order of microseconds. The possible energy transfer mechanisms in the BaSiF₆ matrix codoped with Ce3+ and Tb3+ ions are discussed in the literature, while the influences of doping and crystal size on decay time are obscure.^{7,8} These PL materials could be promising in applications such as color multiplexing,9 temperature sensing,10 biosensing, 11 optical sensing, 12 cell imaging, 13 and photodynamic therapies, 14 etc. BSF is a chemically stable and optically transparent material, 15 and was used as a scintillator for high-energy γ -ray detection. ¹⁶

PL with short radiative decay time is essential for fast optical sensors. ¹⁷ Surface functionalized phosphors with short decay

^a Department of Chemistry and Physics, Fayetteville State University, Fayetteville, NC 28301, USA. E-mail: zluo@uncfsu.edu

^b College of Materials Science and Engineering, Kunming University of Science and Technology, Kunming 650093, P. R. China. E-mail: csufangdong@gmail.com

^c Centre for Nanoscale Materials, Argonne National Laboratory, Argonne, Illinois 60439, USA

^d Oak Ridge Institute for Science and Education, Oak Ridge Associated Universities, Oak Ridge, TN 37830, USA

 $[\]dagger$ Electronic supplementary information (ESI) available: Low-magnification image of BaSiF6 nanowires, EDS results of BaSiF6 and BaF2 nanowires, SEM images of microparticles, proposed mechanisms of nanowire formation, TGA results of BaSiF6 nanowires, PL and PLE spectra of unary doped BaSiF6 and BaF2 nanowires, PL spectra at different doping and excitation, mechanisms of energy transfer, structures of BaSiF6 and BaF2, CIE data and the details on the estimation of the PL decay time. See DOI: 10.1039/c8tc01651h

 $[\]ddagger$ Present address: Southwest Jiaotong University, Chengdu 610031, P. R. China.

time have found applications, such as in biological imaging, ¹⁸ sensing, ^{19,20} drug delivery-discovery, ²¹ clinical diagnosis, ²² energy harvesting, ²³ etc. Currently, fluorescence lifetime imaging is the major application that requires fluorophores with short decay time. ²⁴

Herein, superlong BSF nanowires with high aspect ratios, codoped with Ce³⁺, Tb³⁺, and Eu³⁺ RE ions, were synthesized by a growth-controllable reverse micelle-solvothermal method, and the doping in BSF nanowires was optimized for the best energy transfer bridge between Ce³⁺, Tb³⁺, and Eu³⁺ ions. Furthermore, BSF was decomposed at a high-temperature in a vacuum to yield BaF₂ (BF), a well-known fast scintillator for radiation detection with the shortest decay time of 0.8 ns among all inorganic scintillators.^{25,26} The PL emission and decay time were also compared with the respective microparticle counterparts. These nanowires were further studied using cathodoluminescent (CL) emission spectra under high-energy irradiation. Significantly shortened decay time in subnanosecond has been observed from the codoped high-aspect-ratio BSF nanowires.

Experimental

Sample preparation of pure and doped BaSiF₆ nanowires

All the nanowires were synthesized using a solvothermal method in a quaternary system of cetyltrimethylammonium bromide (CTAB)/water/cyclo-hexane/1-pentanol. All the chemicals were of analytical grade and used without any purification. In the typical process, two identical solutions of 25 mL cyclohexane mixed with 2 g of CTAB (VWR International, LLC.) and 1 mL of 1-pentanol (Sigma Aldrich) were prepared first. To prepare pure BaSiF₆ nanowires, one of the above solutions is added with 1 mL of 1 M BaCl₂·2H₂O (VWR International, LLC.) in water and the other with 1 mL of 1 M SiO₂ (Sigma Aldrich) dissolved in 10% hydrofluoric acid (HF with concentration >40%, Sigma Aldrich). The precursor solutions were added drop wise at a rate of 2 mL h⁻¹ under vigorous stirring at 700 rpm. In this step, both the solutions gradually became transparent. After 30 min of vigorous stirring, both the solutions were mixed together and stirred for another 10 min. The mixed solution was then transferred to 100 mL Teflon-lined autoclaves and heated for 12 h at 120 °C. After 12 h the solution was cooled naturally to room temperature and was washed with ethanol and water several times and dried under vacuum at 80 °C for overnight. The doped nanowires were made using the similar method, in which the respective molar percentages of the RE chlorides CeCl₃, EuCl₃, and TbCl₃ (Beantown Chemical, Hudson) were added to the BaCl₂ solution, and the aforesaid procedure was followed. To obtain nanowires of BaF2, the BaSiF6 nanowires were heated under vacuum at 600 °C for 12 h at a heating rate of 1 °C min⁻¹. The microparticle samples were prepared by direct mixing of 2 mL each of 1 M BaCl₂ solution containing the respective RE chlorides and 1 M SiO2 in 10% HF, followed by heating in an autoclave at 120 °C for 12 h. The doped BaSiF₆ nanowires are represented as BSF:xCe-yTb-zEu and doped BaF2 nanowires as BF:xCe–yTb–zEu, where x, y and z are molar percentages of Ce³⁺, Tb³⁺, and Eu³⁺ ions, respectively, with respect to Ba²⁺ ions.

Characterization

For scanning electron microscopy (SEM) observation and chemical compositional analysis, the samples were coated with ~10 nm carbon and observed on a JEOL field-emission JXA-8530F electron probe microanalyzer (EPMA), equipped with an X-ray energydispersive spectrometer (EDS) for chemical compositional analysis, and a xCLent IV Advanced B Hyperspectral Cathodoluminescence detector for CL spectra. The imaging was done in a SEM mode using the EPMA. Samples for transmission electron microscopy (TEM) were prepared in pure ethanol solutions, sonicated for 30 min to break the long nanowires and then dispersed on carbon-film supported grids. The grids were observed by using an FEI field-emission Tecnai F20ST instrument at 200 kV, and HRTEM was carried out using the Argonne chromatic aberration-corrected TEM (ACAT, a FEI Titan 80-300 ST) with both spherical C_s and chromatic C_c aberration corrections at 200 kV. For EDS mapping, an FEI Talos F200X TEM/STEM instrument was used at 200 kV. The imaging was done in the STEM mode using a high-angle annular dark-field (HAADF) imaging detector, and the elemental maps of selected elements were collected using the X-ray EDS signals. Fourier-transform infrared (FTIR) spectra (Shimadzu IRPrestige-21) were recorded in the transmission mode the KBr pellet method in the wave number range of 300-4000 cm⁻¹ at an average of 32 scans. The stability of nanowires at high temperature was studied using thermogravimetric analysis (TGA) (Shimadzu DTG-60). The X-ray diffraction (XRD) patterns of the samples were obtained using a Rigaku MiniFlex 600 X-ray diffractometer in the scan range of 10-90°. The photoluminescence spectra of the samples were obtained in a powder form using a Shimadzu RF-5301PC spectrofluorophotometer at room temperature. Using an Edinburgh instrument minitau, time-correlated single photon counting (TCSPC) experiments were performed to measure the PL decay dynamics. The samples were excited with 56 ps laser pulses at a wavelength of 405 nm and the emission was monitored at 594 nm. PL decay was detected using a single photon counting photomultiplier tube (PMT). The time resolution of the configuration was \sim 100 ps. The mol% of the dopants in both BSF and BF nanowires is obtained using inductively coupled plasma optical emission spectrometry (ICP-OES, Perkin Elmer 8000).

Results and discussion

Morphology and structure

One-dimensional growth of BSF nanowires is observed with SEM and TEM (Fig. 1a and b) of the samples. A quantitative measurement of the nanowires from the TEM images, without a surface coating, indicates that the average diameter is 35.8 nm with a standard deviation of 5.4 nm, based on 20 measurements. The length is typically in the range of 10–50 μm from low-magnification SEM images (Fig. S1, ESI†), giving the aspect ratio of over several hundreds. A magnified high-resolution

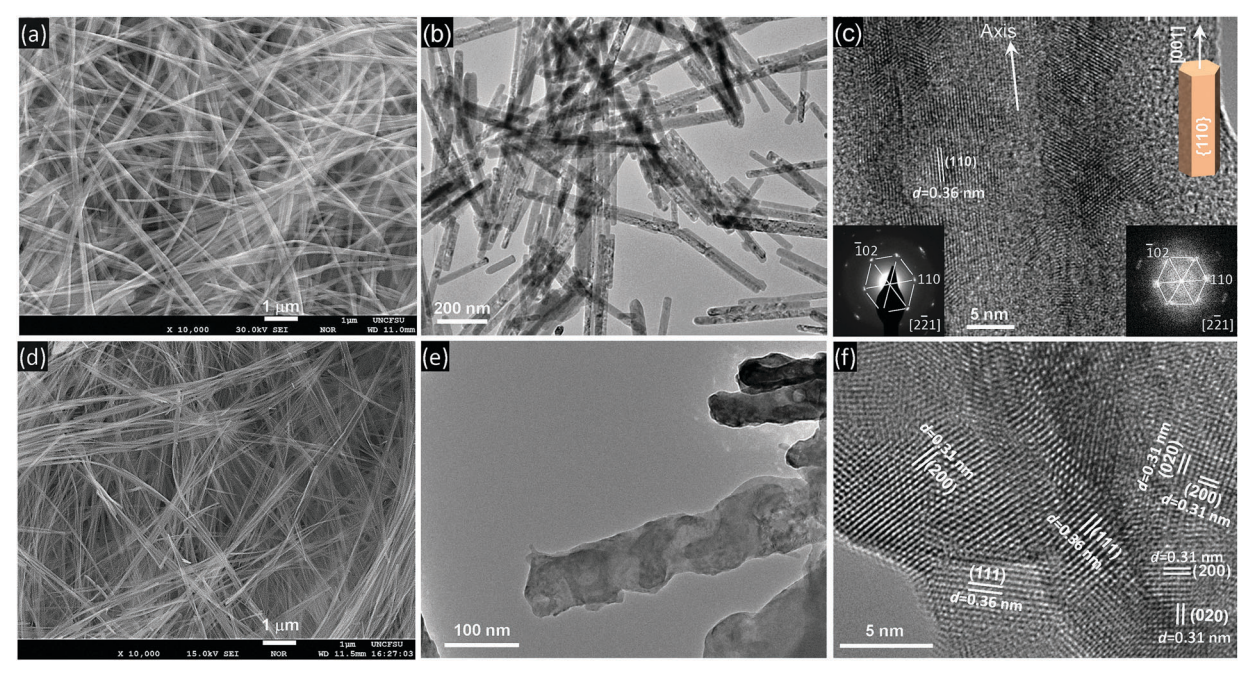


Fig. 1 (a) SEM and (b) TEM images of BSF nanowires; (c) HRTEM image of BSF with SAED (left) and FT (right) patterns inserted; (d) SEM and (e) TEM images of BF nanowires; and (f) HRTEM image of BF nanowire showing nanoparticles.

TEM (HRTEM) image is shown in Fig. 1c, with a selected-area electron diffraction (SAED) pattern inserted showing the nature of a single crystal with a rhombohedral structure within the nanowire. Although the sample is quickly damaged because no surface coating was applied, lattice fringes are still clearly visible, showing {110} planes parallel to the nanowire surfaces. The inserted Fourier transformation (FT) pattern from the HRTEM image is consistent with the SAED pattern from this nanowire. The nanowire axis is along its [001] direction. Such a rhombohedral (or hexagonal) structure facilitates the growth along its c-axis under the controlled conditions. Even though the nanowire morphology of BSF is retained after converting it to BF nanowires (Fig. 1d) under vacuum at 600 °C, BF nanowires are found to be polycrystalline in nature, as evident from TEM and HRTEM images (Fig. 1e and f). The nanowire composition and uniform distribution of the dopants throughout the nanowires are confirmed by EDS mapping (Fig. 2) and point analyses (Fig. S2a and b, ESI†). The size/shape of the nanowires remains unaffected by doping. The SEM images of BSF and BF microparticles are shown in Fig. S3 (ESI†). A proposed mechanism of BSF nanowire formation (Fig. S4, ESI†) is described in the ESI.†

The XRD pattern confirms the pure crystalline nature of BSF nanowires (Fig. 3a) and the sharp peak with extremely high intensity along preferred (110) reflection, demonstrating that the nanowire surfaces are {110}. The XRD patterns of BSF nanowires are indexed as the rhombohedral BaSiF₆ (JCPDS data file No. 15-0736), with a space group of $R\bar{3}m$ and lattice parameters of a = 0.7185 nm and c = 0.7010 nm, consistent with the TEM results. For every Ba²⁺ ion in BSF, the coordination towards fluorine is twelve. The BSF nanowires are stable up to a temperature of 400 °C, as shown from TGA analysis (Fig. S5, ESI†), and then the weight is lost gradually until 600 °C by releasing SiF₄ to derive BaF₂.²⁷ The XRD patterns of BF nanowires are indexed to standard BaF₂ JCPDS data file No. 01-0533 (Fig. 3b), with a space group of $Fm\bar{3}m$ and a lattice parameter of a = 0.62 nm. No impurity phases are observed, indicating that the dopant ions are occupied at the lattice sites of Ba²⁺ ions. However, the charge is compensated between the trivalent RE3+ ions and the divalent Ba2+ ions through defects such as interstitial fluoride ions and/or defect aggregations (cluster formations).²⁸ The actual molar percentages of the dopants in the nanowires with respect to barium ions obtained using ICP-OES are presented in Table S1 (ESI†), which are basically consistent with the nominal compositions. In the Fourier-transform infrared (FTIR) spectra of BSF and BF nanowires, as shown in Fig. 3c, the peaks 725, 498 and 460 cm⁻¹ are assigned to the various vibrations of octahedral SiF₆²⁻ ions²⁹ of BSF, the peak at 375 cm⁻¹ is attributed to the Ba-F stretching of BF, respectively, and the remaining peaks are due to the several vibrational modes of adsorbed water molecules.

Photoluminescence emissions

The PL and photoluminescence excitation (PLE) spectra of codoped BSF and BF nanowires reveal that excitation and emission bands are characteristics to the dopant ions (Fig. 4a, b and Fig. S6, ESI†). In the emission spectrum of Ce³⁺-doped nanowires, a broad peak in the UV region at 335 nm is due to the excitation of electrons from 4f to 5d state and the subsequent relaxation to ground state comprising of a doublet 2F5/2 and ²F_{7/2}, respectively, of Ce³⁺ ions^{30,31} and it is host dependent.³² The spectrum of Eu³⁺ doped nanowires has emissions in the region 570 to 700 nm, which originated from the excited state ${}^{5}D_{0}$ to the ground states ${}^{7}F_{i}$ (j = 0-4); 33 and Tb³⁺ doping results in the sharp peaks noticed at 488, 544, 590 and 620 nm

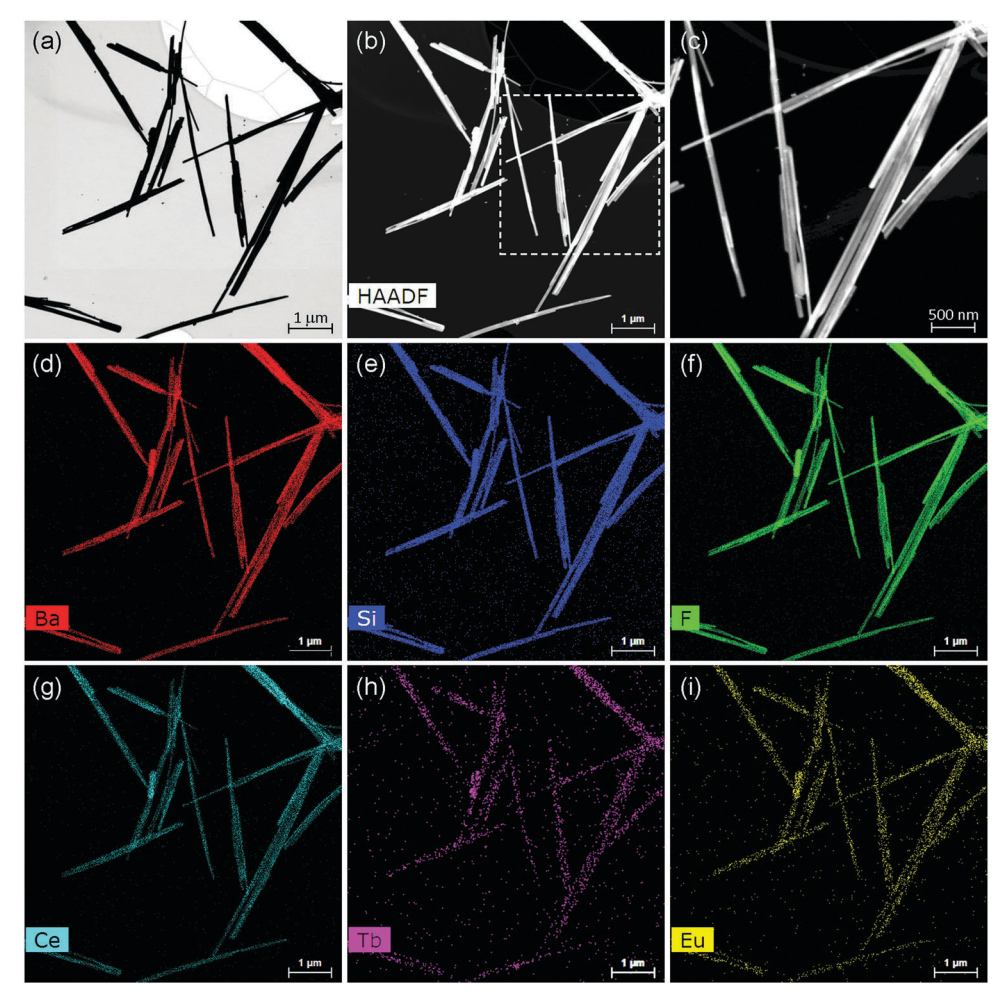


Fig. 2 (a) TEM image of BSF:2Ce-7Tb-5Eu nanowires showing the area for mapping, and (b) corresponding HAADF image. (c) Magnified image from the framed area in (b) showing individual nanowires. (d-i) Elemental maps using EDS showing the distributions of Ba, Si, F, Ce, Tb and Eu, respectively.

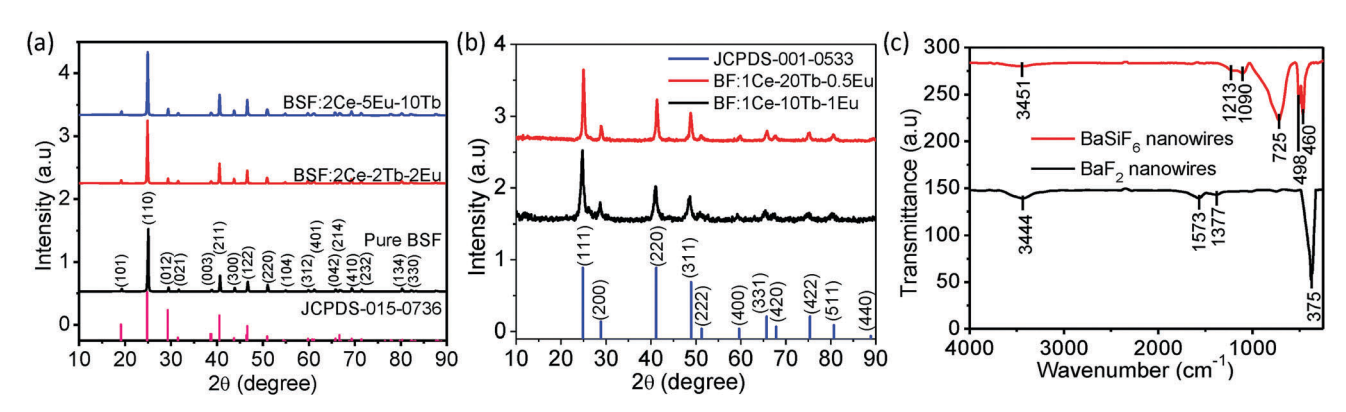


Fig. 3 XRD patterns of representative (a) BSF and (b) BF nanowires; and (c) FTIR spectra of pure BSF and BF nanowires.

originated from ${}^5D_4{}^7F_6$, ${}^5D_4{}^7F_5$, ${}^5D_4{}^7F_4$, and ${}^5D_4{}^7F_3$ 4f–4f transitions of Tb³⁺, respectively.³⁴

In the PLE spectrum monitored at 335 nm emission (Fig. S6, ESI†) of Ce^{3+} doped nanowires, the absorption close to 254 nm corresponds to $5d \rightarrow 4f$ transition of Ce^{3+} ions. On Tb^{3+} doping, a PLE spectrum monitored at 544 nm emission exhibits several bands at 225–400 nm which relates to the $4f^84f^75d^1$ transition

of Tb³⁺ ions.³⁵ In the PLE spectrum of BSF:1Ce-20Tb-1Eu (Fig. 4a), an additional peak appears at 393 nm which is also present in the PLE spectrum of BSF:5Eu (Fig. S6, ESI†), due to Eu³⁺ ions in addition to the 4f⁸4f⁷5d¹ transition of the Tb³⁺ ion. The PLE spectra of codoped samples as shown in Fig. 4a and b exhibit features by adding the PLE spectra of individual unary doped samples as shown in Fig. S6a and b (ESI†).

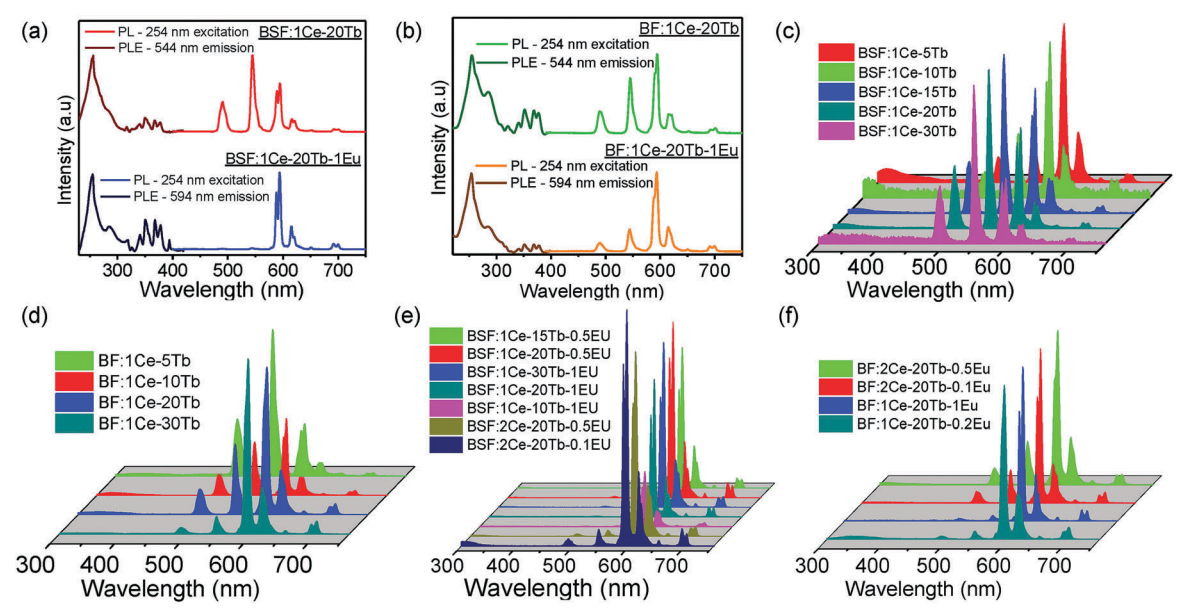


Fig. 4 (a and b) PL and PLE spectra of representative binary- and ternary-doped BSF and BF nanowires; (c) PL spectra of BSF:1Ce-yTb; (d) BF:1Ce-yTb; (e) BSF:xCe-yTb-zEu; and (f) BF:xCe-yTb-zEu nanowire phosphors at 254 nm excitation.

The PL emission spectra of BSF:1Ce–yTb and BF:1Ce–yTb nanowires for an excitation wavelength of 254 nm are shown in Fig. 4c and d, respectively. There is no substantial difference in the emission band positions of BF and BSF nanowires doped with Ce^{3+} and Tb^{3+} ions. Fig. S7 (ESI†) also shows the PL emission from binary-doped samples.

In general, the emission lines from both Ce^{3^+} and Tb^{3^+} doped BSF and BF nanowires are consistent with the sum of emissions from singly-doped nanowires, but the intensity of emissions from binary-doped nanowires is significantly improved by the presence of Ce^{3^+} ions. The emission line arising from Ce^{3^+} ions near 335 nm is negligible as compared with the emissions from Tb^{3^+} ions, indicating the complete energy transfer between those ions. On a close observation, when BSF nanowires doped with Ce^{3^+} and Tb^{3^+} ions, the dominant emission line is at 544 nm, whereas it is at 590 nm in all BF nanowires. This difference in the emission intensity of BSF and BF nanowires is in connection with the symmetry of dopant sites in the respective lattices. In BSF, the dopants replace Ba^{2^+} ions with a D_{3d} point symmetry; 36 however, in BF the dopants occupy lattice sites of Ba^{2^+} ions with a cubic symmetry (Fig. S8, ESI†).

As shown in Fig. 4e and f, both BSF and BF nanowires display strong emission lines at 594 and 615 nm, corresponding to the emission from Eu^{3+} ions, originating from $^5D_0 \rightarrow {}^7F_j$ (j=1,2) transitions, respectively. Intensity of the emission in orange-red region is increased significantly by the addition of Tb^{3+} ions while the concentrations of Ce^{3+} and Eu^{3+} are kept constant. The emission line at 335 nm appears when the Ce^{3+} concentration is 2% while that of Eu^{3+} is 0.5% (Fig. S9a and b, ESI†). The characteristic emissions of doped BF nanowires are akin to those of BSF nanowires, besides the superior emissions arising from the Tb^{3+} ions as compared with those in BSF matrix, which can be attributed to reordering the dopant ions in the lattice with less structural defects after heating

at 600 °C. The emission at 594 nm ($^5D_0 \rightarrow {}^7F_1$) is associated with a magnetic dipole transition and the emission at 615 nm ($^5D_0 \rightarrow {}^7F_2$) is due to electronic dipole transition.

The magnetic dipole transition dominates when Eu^{3+} is situated at a site coinciding with a center of symmetry, and an electronic dipole transition prevails when Eu^{3+} ions occupy a site which lacks an inversion symmetry. Since the intensity of the 594 nm peak is higher than the 615 nm peak, one can confirm that the Eu^{3+} ions occupy the site of Ba^{2+} ions in BSF with a center of symmetry. The peak intensity ratio between $\binom{5}{D_0} \rightarrow \binom{7}{F_2}$ and $\binom{5}{D_0} \rightarrow \binom{7}{F_1}$ transition is a measure of distortion around the Eu^{3+} ions. On comparing above ratios of BSF:5Eu and BSF:xCe-yTb-5Eu, it is concluded that the doping of Ce^{3+} and Tb^{3+} does not alter the neighborhood of Eu^{3+} ions, as there is no significant difference in the same. In contrary, the 594 nm and 615 nm emission ratios of BF nanowires are higher than that of BSF nanowires, indicating a difference in the symmetry of the dopant sites in the respective crystal lattices.

From the PLE spectra, the excitation of binary- and ternary-doped BSF nanowires is possible by a 376 nm source (Fig. 5), with a broad blue emission originating from Tb^{3+} ions assigned to the transitions ${}^5\mathrm{D}_0 \to {}^7\mathrm{F}_j$ (j=0,1,2,3,4) due to the relaxation of the ions excited by the direct source band and sharp orange-red emission bands corresponding to the transition ${}^5\mathrm{D}_0 \to {}^7\mathrm{F}_j$ (j=0,1,2,3,4) of Eu^{3+} ions. The resultant CIE coordinates are presented in Fig. S10 and Table S2 (ESI†). A slight change in the Eu^{3+} doping can bring an appreciable change in the emission and the dopant ratio can be optimized to attain blue, red, and white light emissions. The energy transfer mechanism is discussed in the ESI.†

The luminescence emissions of nanowires and microparticles are compared and shown in Fig. S11 (ESI†). The fluorescence emission bands of both the samples are the same but the

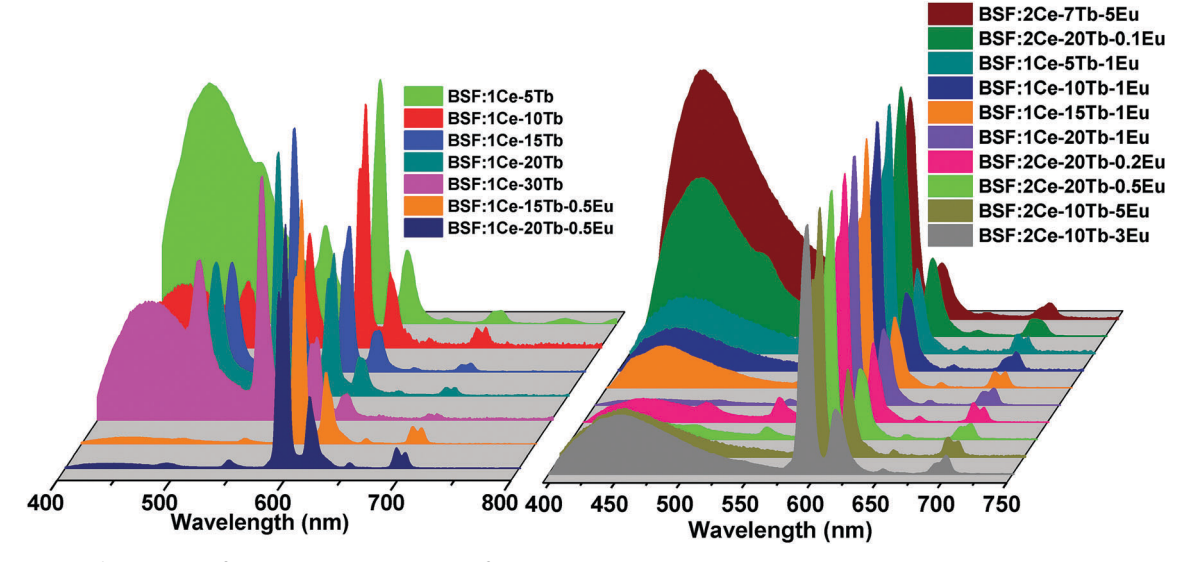


Fig. 5 PL spectra of codoped BaSiF₆ nanowires excited by 376 nm wavelength.

emissions from nanowires are intensified compared to microparticles though doped with the same ratio of RE ions, due to their increased surface area with more active dopants on the surfaces.

Photoluminescence decay dynamics

The time-resolved PL decay dynamics of representative codoped BSF and BF nanowires for the emission at 594 nm (corresponding to ${}^5\mathrm{D}_4 \to {}^7\mathrm{F}_4$ of Tb^{3+} ions in binary xCe-yTb, or ${}^5\mathrm{D}_0 \to {}^7\mathrm{F}_1$ transitions of Eu³⁺ ions in ternary xCe-yTb-zEu doped nanowires) are shown in Fig. 6a and b, and the overall decay time and the parameters for the remaining nanowires are listed in Table 1. The decay time curves can be fitted to a double exponential and the equations used in the estimation of decay time are presented in the ESI.† The fast (τ_1) and slow (τ_2) decay time components of the samples are perhaps due to two different recombination centers of Tb3+ or Eu3+ ions: one on the distorted lattice sites close to the surface and the other from the bulk of the nanowires.³⁸ On a comparison made among the decay times of different Tb³⁺ contents (Table 1) in BSF:xCe-yTb and BSF:xCe-yTb-zEu nanowires, the decay time is decreased monotonically with increasing Tb3+ concentrations, which strongly supports the energy transfer from Ce³⁺ to Tb³⁺ ions, considering the fact that the contribution from cross relaxation to nonradiative relaxation increases with increasing concentration which ultimately decreases the decay time of activators.³⁹ The lowest decay time is expected for optimal Ce^{3+} and Tb^{3+} contents with maximum energy transfer. 40 The decay times in ternarydoped nanowires are shorter than binary-doped ones because of the energy exchange between Ce3+, Tb3+, and Eu3+ ions, as a result, rapid relaxation of the excited ions can take place through more different pathways than binary-doped samples.

The PL decay time recorded for these nanowires is shorter than the decay time reported in the literature, due to the dopant occupancy in the lattice sites and crystal size effects. ^{41–43} The PL transitions from dopants occupying the center of symmetry

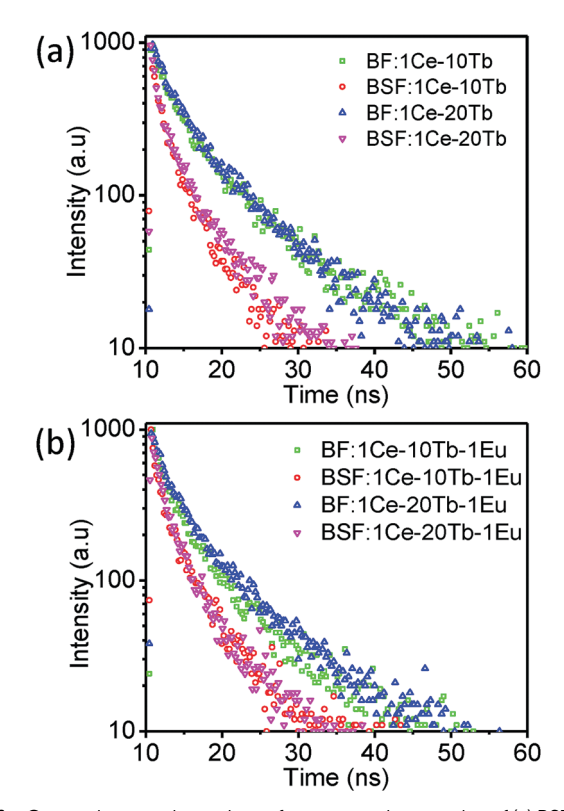


Fig. 6 Comparison on decay time of representative samples of (a) BSF:1Ce-yTb and BF:1Ce-yTb, and (b) BSF:1Ce-yTb-1Eu and BF:1Ce-yTb-1Eu.

(like BSF) has a faster decay time, whereas the one occupying the lattice sites with inversion symmetries (like BF) has a slower decay time. In Mn⁴⁺ doped BSF, the Mn⁴⁺ ions occupying the Si⁴⁺ site in BSF have a $^2E_g^4E_{2g}$ spin- and parity-forbidden transition with a slow decay time of ~ 6.5 ms (monitored at 634 nm emission), whereas, the RE dopants occupy Ba²⁺ sites in BSF, and the decay time is significantly shortened, *e.g.*, Pr³⁺-doped BSF powder with 70 ns decay time when excited by a 187 nm

Table 1 Parameters of exponential fits and average decay times of codoped BSF and BF nanowires

Sample	τ_1 (ns)	τ_2 (ns)	α_1	$lpha_2$	Adj. R^2	τ_{avg} (ns)
BSF:1Ce-10Tb	0.92	4.77	4.45×10^{8}	2922.74	0.9949	0.92
BSF:1Ce-20Tb	0.88	5.28	$5.31 imes 10^8$	2452.88	0.9944	0.88
BSF:1Ce-5Tb-1Eu	1.02	5.98	2.34×10^{7}	1779.38	0.9957	1.02
BSF:1Ce-10Tb-1Eu	0.9	5.56	8.73×10^{7}	1956.85	0.9943	0.9
BSF:1Ce-20Tb-1Eu	0.82	5.94	1.01×10^7	1602.17	0.996	0.82
BSF:1Ce-30Tb-1Eu	0.81	5.25	3.16×10^8	2146.58	0.995	0.81
Micro-BSF:1Ce-20Tb	1.81	90.81	$3.23 imes 10^5$	76.78	0.9853	1.81
Micro-BSF:1Ce-20Tb-1Eu	1.78	150.53	1258.17	71.39	0.9876	1.78
BF:1Ce-10Tb	2.38	9.89	$5.95 imes 10^4$	1035.51	0.9964	2.38
BF:1Ce-20Tb	2.1	10.18	1.13×10^{5}	7371.52	0.9953	2.1
BF:1Ce-10Tb-1Eu	1.69	8.6	3.56×10^{5}	1338.96	0.9946	1.69
BF:1Ce-20Tb-1Eu	1.48	8.34	9.54×10^{5}	1190.09	0.9946	1.48
Micro-BF:1Ce-20Tb	2.5	17.71	$5.65 imes 10^4$	292.76	0.9892	2.5
Micro-BF:1Ce-20Tb-1Eu	1.52	9.61	7.99×10^{5}	1200.72	0.9929	1.62

source and the emission monitored between 200-450 nm. 37 The size effect on decay time is also prevalent. ⁴³ The fast component τ_1 of the decay time for BSF microparticles is increased by nearly two times and the slow component τ_2 is increased ~17 times in BSF:1Ce-20Tb and ~25 times in BSF:1Ce-20Tb-1Eu, respectively, in comparison with the corresponding nanowires. The fact that the slow component of microparticles is longer than that of BSF nanowires confirms the assumption of its origin from the bulk of the sample. The effect of deep traps on the bulk of nanowires is trivial due to increased surface defects, whereas in microparticles the deep traps dominate over the surface defects. 44 In BF microparticles, τ_1 and τ_2 of nanowires are increased only by a small fraction compared with the BF nanowires, and the average decay time of the BF samples is approximately 1.5-2 ns. Yet another study on Nd³⁺-doped BaF₂ nanoparticles showed a decay time of 350-900 ns whereas the decay time of the polycrystalline sample was 3000 ns (excited at 488 nm and emission monitored at 1052 nm). 45 The decay time reported for BaF_2 bulk doped with Ce^{3+} ions is ~ 27 ns (excited by a 289 nm source and emission monitored at 323 nm), 46 and with Pr3+ ions is \sim 20 ns (excited by a 205 nm source and emission monitored at 230 nm). 47 The present nanowires exhibit a short decay time due to the presence of surface traps, which actually can transfer the energy to luminescent centers.48

The average decay time of BSF nanowires is shorter than that of BF nanowires. The dopant ions in BF are more symmetric (cubic symmetry) than the one in BSF lattices (D_{3d} point symmetry) and the forbidden f-f transitions are favorable for dopants at a lower symmetry site, hence one can expect a shorter decay time.⁴⁹

On accounting the phonon energy of the lattices, the lattice distortions can increase the phonon energy. The non-radiative relaxations of RE ions are influenced by the phonon frequencies of the host lattices. The reciprocal of decay time, τ is determined by radiative emission, nonradiative relaxation and cross relaxation between the adjacent ions. Therefore the total relaxation rate can be expressed as (eqn (1))

$$\tau^{-1} = \sum \tau_{NR}^{-1} + \sum \tau_{R}^{-1} + P_{CR}$$
 (1)

where $\sum \tau_R^{-1}$ is the radiative (photon) emission rate and $\sum \tau_{NR}^{-1}$ is the nonradiative (multiphonon) emission rate. The term PCR is the rate of cross relaxation between the adjacent ions.

The decay time of BSF and BF samples doped with the same composition of RE elements and the contribution from PCR are assumed to be the same and hence, $\sum \tau_R^{-1}$ and $\sum \tau_{NR}^{-1}$ are the major factors contributing to the decay time. $\sum \tau_{NR}^{-1}$ is dependent on the site symmetry and environment of the dopant ions whereas $\sum \tau_{NR}^{-1}$ is determined by the lattice phonon energy. Therefore, the decay time can be changed either by the local symmetry of the RE ion in the host lattice or by the phonon energy of the host, unless the level of doping is changed. 51

The non-radiative relaxation is, in turn, related to the number of phonons as in eqn (2),

$$\tau_{\rm NR}^{-1} = A \exp(-Bp) \tag{2}$$

where A and B are constants, p is the number of phonons which can be calculated using eqn (3),

$$p = \Delta E/\hbar\omega \tag{3}$$

where $\Delta E = 16\,835~{\rm cm}^{-1}$ (corresponding to the fluorescence at 594 nm, the energy gap corresponding to the transitions ${}^5{\rm D}_4 \rightarrow {}^7{\rm F}_4$ of Tb³⁺ and ${}^5{\rm D}_0 \rightarrow {}^7{\rm F}_1$ of Eu³⁺ ions, respectively) and $\hbar\omega$ is the energy of phonons, in wave numbers, of the crystal lattice.

The lattice phonon energy, $\hbar\omega$, can be approximated to the lowest vibration energies in the IR spectra of BSF and BF and are 480 and 375 cm⁻¹, respectively. The corresponding number of phonons is 35 and 45 for BSF and BF, respectively. From eqn (1), one can conclude that with an increase in the number of phonons p, $\sum \tau_{\rm NR}^{-1}$ decreases and as a result the decay time increases. Hence it is recognized that the difference in the luminescence decay time among BSF and BF doped samples can be accompanied to the difference in the radiative and nonradiative relaxation mechanisms associated with the crystal structure of the host matrix and the phonon energy of the host. To be precise, there exists competition between the radiative and nonradiative decay rates. ⁵²

Cathodoluminescence characteristics

The CL spectra of the codoped BSF and BF nanowires and microparticles are recorded using high-energy electrons to excite scintillation for radiation detection,⁵³ and representative

CL spectra are shown in Fig. 7. Both pure BSF and BF nanowires exhibit strong CL emissions in the visible range. The CL spectrum of pure BSF nanowires is intense with broad bands at 390 and 510 nm, respectively, whereas pure BF nanowires exhibit a broad band at 390 nm. The common peak at 390 nm (3.18 eV) in the CL spectra of both BSF and BF nanowires implies that it has the same origin, from the $2p\ F^- \to 5p\ Ba^{2+}$ cross-over transition of electrons, 54 which is in turn due to the holes generated in cations during their ionization by the high energy source. The band at 510 nm (2.43 eV) from BSF nanowires is conceived as the radiative recombination of the self-trapped excitons (STE), the electron–hole pairs restricted by a self-induced lattice distortion, and the radiative relaxation restores the original defect-free structure. 55

While comparing the CL emissions from the doped and pure nanowires, the emissions from Tb³⁺ doped nanowires are similar to those of pure BSF nanowires, as shown in Fig. 7a. However, weak characteristic emissions from Tb³⁺ ions appear in the presence of Ce³⁺ ions from BSF:1Ce-15Tb nanowires, indicating an energy transfer between the ions. The energy transfer is also observed in BSF:1Ce-20-Tb-1Eu nanowires with the characteristic emissions from Eu³⁺ ions. In doped BF nanowires, as shown in Fig. 7b, an ample improvement in CL emissions is observed compared to BSF nanowires especially due to the presence of Ce³⁺ ions as in BF:1Ce-15Tb and BF:1Ce-20Tb-1Eu nanowires. Therefore, one can conclude that the energy from the cross-over transition excites the Ce³⁺ ions and the energy transfer from Ce³⁺ ions subsequently excites Tb³⁺/Eu³⁺ ions. An effective energy transfer is not found in codoped BSF nanowires, in which the energy transfer is partial due to the presence of STEs.

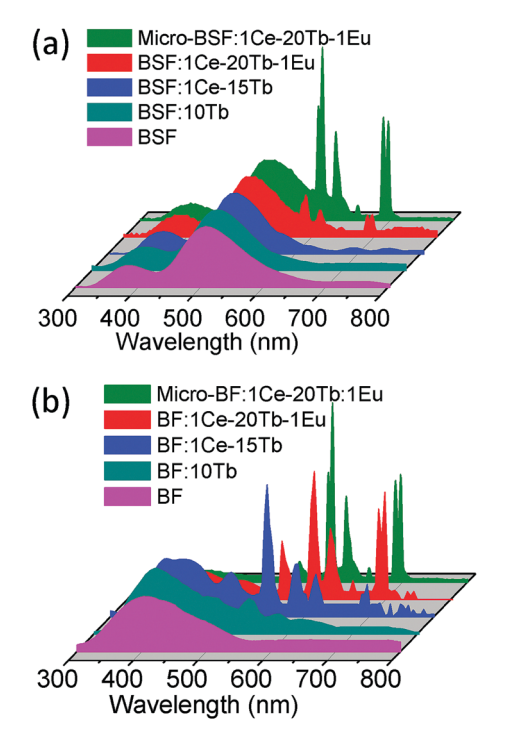


Fig. 7 Cathodoluminescence emission of pure and unary doped (a) BSF and (b) BF nanowires.

The CL emissions from the micro-sized particles are superior to the nanowires. In nanowires, the mean-free path of the electron/hole ($\sim 30\,$ nm) and the size of the nanowires are comparable, therefore, the charge carriers can be either captured by the surface defects or leave the nanoparticles. ⁵⁶ As a result, luminescence quenching-induced low luminescence intensities are apparent from nanowires as against microparticles. Strong characteristic emissions from the dopants are observed in the CL spectrum of microparticles as compared to the same noticed from the nanowires. Hence, it is concluded that the CL emission also follows the energy transfer mechanism observed in photoluminescence and the ions are excited by the energy associated with the transitions of the lattice.

Conclusions

In summary, photoluminescent and cathodoluminescent RE ion-doped BaSiF₆ nanowires were synthesized using a growthcontrolled solvothermal method, and annealing the BaSiF₆ nanowires at 600 °C under vacuum yielded BaF2 nanowires. TEM and XRD analyses of these nanowires were conducted. The influence of various doping of Ce³⁺, Tb³⁺, and Eu³⁺ RE ions on the photoluminescence of BaSiF₆ and BaF₂ nanowires was studied. The PL monitored when excited by a 254 nm source is associated with the respective energy transfer between Ce³⁺-Tb³⁺-Eu³⁺ ions. The doped nanowires excited by a 376 nm source also could produce a wide emission in the visible range. The decay time of codoped BaSiF₆ nanowires was found to be shorter than that of codoped BaF₂ nanowires. Codoping with Ce³⁺-Tb³⁺-Eu³⁺ provides an efficient way to shorten the decay time of BaF₂ with visible emissions. With intense emissions in the visible range with a short decay time, these easy-grown and superlong nanowires with high aspect ratios may be used for fast luminescence sensing applications.

Authors' contributions

G. George conducted the sample synthesis and PL measurements, and prepared the manuscript; S. L Jackson and Z. R. Mobley conducted the sample processing and preparation; B. R. Gautam conducted the decay dynamics; D. Fang attended the experimental design and data analysis; J. Peng, D. Luo and J. Wen conducted the TEM work; J. E. Davis and D. Ila conducted the research on scintillation; and Z. Luo designed the experiment, conducted the EPMA/CL measurement and revised the manuscript.

Conflicts of interest

There are no conflicts to declare.

Acknowledgements

The authors would like to gratefully acknowledge the National Science Foundation for research funding, award no. HRD 1436120 and 1719511, and ORAU-Directed Research and Development Grant.

The instrumentation was supported by the U.S. Department of Defense grants W911NF-14-1-0060, W911NF-15-1-0566 and W911NF-09-1-0011, and NSF MRI Program DMR 1626376. Use of the Center for Nanoscale Materials, an Office of Science user facility, was supported by the U.S. Department of Energy, Office of Science, Office of Basic Energy Sciences, under Contract No. DE-AC02-06CH11357.

References

- 1 J. Zhou and Z. Xia, J. Mater. Chem. C, 2015, 3, 7552-7560.
- 2 Y. Huang, H. You, G. Jia, Y. Song, Y. Zheng, M. Yang, K. Liu and N. Guo, J. Phys. Chem. C, 2010, 114, 18051–18058.
- 3 D. Sekiguchi, J. Nara and S. Adachi, *J. Appl. Phys.*, 2013, 113, 183516.
- 4 Q. Zhou, Y. Zhou, Y. Liu, L. Luo, Z. Wang, J. Peng, J. Yan and M. Wu, *J. Mater. Chem. C*, 2015, 3, 3055–3059.
- 5 D. Sekiguchi and S. Adachi, ECS J. Solid State Sci. Technol., 2014, 3, R60–R64.
- 6 R. Hoshino, T. Nakamura and S. Adachi, ECS J. Solid State Sci. Technol., 2016, 5, R37–R43.
- 7 Y. Zhang, L. Yuan, K. Huang, Y. Du and S. Feng, New J. Chem., 2015, 39, 9071–9074.
- 8 Y. Zhang, X. Zhong, L. Yuan, K. Huang and S. Feng, J. Lumin., 2018, 198, 203–207.
- 9 H. Dong, L.-D. Sun, W. Feng, Y. Gu, F. Li and C.-H. Yan, ACS Nano, 2017, 11, 3289–3297.
- D. Ananias, F. A. A. Paz, D. S. Yufit, L. D. Carlos and J. Rocha, J. Am. Chem. Soc., 2015, 137, 3051–3058.
- 11 A. Pratsinis, G. A. Kelesidis, S. Zuercher, F. Krumeich, S. Bolisetty, R. Mezzenga, J.-C. Leroux and G. A. Sotiriou, ACS Nano, 2017, 11, 12210–12218.
- 12 A. Lay, D. S. Wang, M. D. Wisser, R. D. Mehlenbacher, Y. Lin, M. B. Goodman, W. L. Mao and J. A. Dionne, *Nano Lett.*, 2017, 17, 4172–4177.
- 13 G. A. Sotiriou, D. Franco, D. Poulikakos and A. Ferrari, ACS Nano, 2012, 6, 3888–3897.
- 14 A. Kamkaew, F. Chen, Y. Zhan, R. L. Majewski and W. Cai, *ACS Nano*, 2016, **10**, 3918–3935.
- 15 G. Wang, W. Qin, D. Zhang, G. Wei, K. Zheng, L. Wang and F. Ding, *J. Fluorine Chem.*, 2009, **130**, 755–758.
- 16 J. M. Bewers and F. C. Flack, *Nucl. Instrum. Methods*, 1968, **59**, 337–338.
- 17 X. Wang and O. S. Wolfbeis, *Chem. Soc. Rev.*, 2014, 43, 3666–3761.
- 18 M. Y. Berezin and S. Achilefu, *Chem. Rev.*, 2010, **110**, 2641–2684.
- 19 A. Orte, J. M. Alvarez-Pez and M. J. Ruedas-Rama, ACS Nano, 2013, 7, 6387–6395.
- 20 T. Zhou, T. Luo, J. Song and J. Qu, *Anal. Chem.*, 2018, **90**, 2170–2177.
- 21 M. Bardhan, A. Majumdar, S. Jana, T. Ghosh, U. Pal, S. Swarnakar and D. Senapati, *J. Photochem. Photobiol., B*, 2018, **178**, 19–26.

- 22 J. S. Basuki, H. T. T. Duong, A. Macmillan, R. B. Erlich, L. Esser, M. C. Akerfeldt, R. M. Whan, M. Kavallaris, C. Boyer and T. P. Davis, ACS Nano, 2013, 7, 10175–10189.
- 23 S. Kundu and A. Patra, Chem. Rev., 2017, 117, 712-757.
- 24 R. W. K. Leung, S.-C. A. Yeh and Q. Fang, *Biomed. Opt. Express*, 2011, **2**, 2517–2531.
- 25 W. W. Moses, M. J. Weber, S. E. Derenzo, D. Perry, P. Berdahl and L. A. Boatner, *IEEE Trans. Nucl. Sci.*, 1998, 45, 462–466.
- 26 M. Laval, M. Moszyński, R. Allemand, E. Cormoreche, P. Guinet, R. Odru and J. Vacher, *Nucl. Instrum. Methods Phys. Res.*, 1983, 206, 169–176.
- 27 C. J. Hoffman and H. S. Gutowsky, *Inorg. Synth.*, 1953, 4, 145–146.
- 28 C. Lorbeer, F. Behrends, J. Cybinska, H. Eckert and A.-V. Mudring, *J. Mater. Chem. C*, 2014, 2, 9439–9450.
- 29 R. B. Badachhape, G. Hunter, L. D. McCory and J. L. Margrave, *Inorg. Chem.*, 1966, 5, 929–931.
- 30 Y.-C. Lin, P. Erhart, M. Bettinelli, N. C. George, S. F. Parker and M. Karlsson, *Chem. Mater.*, 2018, **30**, 1865–1877.
- 31 Z. L. Wang, Z. W. Quan, P. Y. Jia, C. K. Lin, Y. Luo, Y. Chen, J. Fang, W. Zhou, C. J. O'Connor and J. Lin, *Chem. Mater.*, 2006, 18, 2030–2037.
- 32 B. F. Aull and H. P. Jenssen, *Phys. Rev. B: Condens. Matter Mater. Phys.*, 1986, 34, 6640-6646.
- 33 F. Du, Y. Nakai, T. Tsuboi, Y. Huang and H. J. Seo, *J. Mater. Chem.*, 2011, **21**, 4669–4678.
- 34 N. Souri, P. Tian, C. Platas-Iglesias, K.-L. Wong, A. Nonat and L. J. Charbonnière, *J. Am. Chem. Soc.*, 2017, 139, 1456–1459.
- 35 C. Duan, Z. Zhang, S. Rösler, S. Rösler, A. Delsing, J. Zhao and H. T. Hintzen, *Chem. Mater.*, 2011, 23, 1851–1861.
- 36 E. van der Kolk, P. Dorenbos, C. W. E. van Eijk, A. P. Vink, C. Fouassier and F. Guillen, *J. Lumin.*, 2002, **97**, 212–223.
- 37 J. J. H. A. van Hest, G. A. Blab, H. C. Gerritsen, C. de Mello Donega and A. Meijerink, *J. Phys. Chem. C*, 2017, 121, 19373–19382.
- 38 G. Zatryb, A. Podhorodecki, J. Serafińczuk, M. Motyka, M. Banski, J. Misiewicz and N. V. Gaponenko, *Opt. Mater.*, 2013, 35, 2090–2094.
- 39 S. Saha, P. S. Chowdhury and A. Patra, *J. Phys. Chem. B*, 2005, **109**, 2699–2702.
- 40 L. Wang, R.-J. Xie, T. Suehiro, T. Takeda and N. Hirosaki, *Chem. Rev.*, 2018, **118**, 1951–2009.
- 41 C. R. Ronda, in *Luminescence*, ed. C. Ronda, Wiley-VCH Verlag GmbH & Co., KGaA Weinheim, 2007, ch. 1, pp. 1–34.
- 42 C. Altavilla, Upconverting Nanomaterials: Perspectives, Synthesis, and Applications, CRC Press, Boca Raton, 2016.
- 43 Z. Luo, J. G. Moch, S. S. Johnson and C. C. Chen, *Curr. Nanosci.*, 2017, **13**, 364–372.
- 44 X. Duan, L. Yi, X. Zhang and S. Huang, *J. Nanomater.*, 2015, 298692.
- 45 C. M. Bender, J. M. Burlitch, D. Barber and C. Pollock, *Chem. Mater.*, 2000, **12**, 1969–1976.

- 46 R. Visser, P. Dorenbos, C. W. E. van Eijk, A. Meijerink, G. Blasse and H. W. den Hartog, *J. Phys.: Condens. Matter*, 1993, 5, 1659–1680.
- 47 C. Pédrini, D. Bouttet, C. Dujardin, B. Moine and H. Bill, *Chem. Phys. Lett.*, 1994, **220**, 433–436.
- 48 X. Zhang, J. Zhang, X. Zhang, M. Wang, H. Zhao, S. Lu and X. Wang, *J. Phys. Chem. C*, 2007, **111**, 18044–18048.
- 49 S. J. Fancey, G. S. Buller, J. S. Massa, A. C. Walker, S. D. Perrin, A. J. Dann and M. J. Robertson, *J. Cryst. Growth*, 1998, **183**, 269–273.
- 50 F. Zhang, S.-W. Chan, J. E. Spanier, E. Apak, Q. Jin, R. D. Robinson and I. P. Herman, *Appl. Phys. Lett.*, 2002, 80, 127–129.

- 51 A. Patra, Solid State Commun., 2004, 132, 299-303.
- 52 W. Chen, X. Wen, J. Yang, M. Latzel, R. Patterson, S. Huang, S. Shrestha, B. Jia, D. J. Moss, S. Christiansen and G. Conibeer, *Nanoscale*, 2018, 10, 5358–5365.
- 53 I. H. Campbell and B. K. Crone, *Adv. Mater.*, 2005, **18**, 77–79.
- 54 Y. A. Valbis, Z. A. Rachko and Y. L. Yansons, *JETP Lett.*, 1985, **42**, 172–174.
- 55 M. A. S. Kalceff, *Phys. Rev. B: Condens. Matter Mater. Phys.*, 1998, 57, 5674–5683.
- 56 V. V. Vistovskyy, A. V. Zhyshkovych, O. O. Halyatkin, N. E. Mitina, A. S. Zaichenko, P. A. Rodnyi, A. N. Vasil'ev, A. V. Gektin and A. S. Voloshinovskii, *J. Appl. Phys.*, 2014, 116, 05430.